

# Effect of external reflectors on radiation profile of grating coupled surface emitting lasers

S.F. Yu  
L.M. Zhang  
R.G.S. Plumb  
J.E. Carroll

*Indexing terms: External reflectors, Radiation profile, Surface emitting lasers*

**Abstract:** Grating coupled surface emitting distributed feedback lasers are analysed by our recently developed model. The model takes into account spontaneous emission, the longitudinal variation of carrier concentration and that of photon density, calculated by a self-consistent technique. The emission spectrum and near and far field radiation patterns are determined as a function of the injection current and external optical feedback. It is found that a single lobed far field radiation pattern is favoured by asymmetric coating of the facets. In addition, the phase margin to achieve a single lobed radiation profile can be increased by increasing the amplitude of the reflection

## Parameters used in the model

Biomolecular carrier recombination coefficient, $B$	$1 \times 10^{-10} \text{ cm}^3 \text{ s}^{-1}$
Auger carrier recombination coefficient, $C$	$3 \times 10^{-29} \text{ cm}^6 \text{ s}^{-1}$
Differential gain, $a$	$3 \times 10^{-16} \text{ cm}^2$
Nonlinear gain coefficient, $\varepsilon$	$1.7 \times 10^{-17} \text{ cm}^3$
Transparency carrier density, $N_0$	$1.5 \times 10^{18} \text{ cm}^{-3}$
Effective phase refractive index, $n_{eff0}$	3.28
Linewidth enhancement factor, $\alpha_H$	4.86
Absorption and scattering loss, $\alpha$	$40 \text{ cm}^{-1}$
Length of laser cavity, $L$	$400 \mu\text{m}$
Coupling coefficient $K$	$50 \text{ cm}^{-1}$
Active layer thickness, $d$	$0.18 \mu\text{m}$
Waveguide confinement factor, $\Gamma$	0.35
Approximate emission wavelength, $\lambda_0$	$1.55 \mu\text{m}$
Period of grating, $\Lambda$	$0.45 \mu\text{m}$

## 1 Introduction

Grating coupled (GC) surface emitting diode lasers use gratings (usually second order) to provide longitudinal feedback and first order radiation in the transverse direction. Two types of GC surface emitting lasers have been extensively analysed [1-4], namely surface emitting dis-

tributed feedback (SEDFB) lasers and surface emitting distributed Bragg reflector (SEDBR) lasers. In a surface emitting DFB laser, the gain region and grating are parallel along the laser cavity [5, 6]. However, in a surface emitting DBR laser, DBR sections and gain sections are cascaded in the longitudinal direction [7], usually on a common waveguide. Monolithic one-dimensional or two-dimensional phase locked arrays can also be fabricated [8, 9]. Surface radiation originates from DBR sections and the array is pumped by the intervening gain regions.

The above devices are usually designed for low beam divergence and high power radiation. The radiation efficiency of the SEDFB lasers can be enhanced by cleaved facets [6] or by strong longitudinal carrier confinement [5, 6]. In addition, SEDBR laser arrays with phase locked operation further increase both the maximum radiated power and the ability to control beam divergence. For SEDBR lasers, a minimum beam divergence of  $0.012^\circ$  [10] and radiated power of more than one Watt [11] have been demonstrated experimentally.

Besides using GC surface emitting lasers as high power lasing sources with high quality beam profiles, the second order grating can also be employed as a passive surface emitting beam deflector [12, 13] in optical interconnects between wafers [14, 15] (chip to chip interconnection) or parallel optical signal processing [16]. Modified SEDFB laser structures can also be used as two state optical switches, analogous to the passive structures of reference [17]. The advantage of active devices is that no external optical source is required, and hence the optical system is compact.

It has been shown that, in DBR surface emitting arrays [3, 8, 9], the radiation profile from the DBR sections can be controlled by differential current injection into the different gain sections, and distinctively different far field profiles can be obtained. This is because the non-uniform current injection alters the resonant optical profile within the array. Similar alteration can be achieved in a single SEDFB laser by splitting its metal contact into two (or more) sections, and driving these separately. The nonuniform current injection alters the lasing frequency [18] of the laser slightly as well as

The authors would like to thank M. Robertson from BTL for supplying the laser diode, R. Crane for help with the experimental setup and C. Tsang for his project report. One of the authors (S. Yu) also wishes to thank the Croucher Foundation of Hong Kong and ORS Award for support.

Paper 9275J (E3, E13), first received 22nd May and in revised form 22nd October 1992

The authors are with the Department of Engineering, Cambridge University, Trumpington Street, Cambridge CB2 1PZ, United Kingdom

changing the radiated beam profile. Two distinct far field profiles (single and double lobed) can be exhibited in such a SEDFB laser which may therefore be used as an active two state switch.

In this paper, the SEDFB laser is analysed using the power matrix method [19]. In the calculation, we use the usual coupled mode equations including longitudinal variations of electron density and refractive index due to spatial hole burning. Gain saturation effects are also included. The longitudinal variations inside the laser are dealt with by splitting the laser into a number of sections, each of which is spatially uniform. Spontaneous emission is introduced at the boundary between each pair of sections.

In the following paragraphs, the SEDFB laser is assumed to be uniformly injected. The radiation pattern and the wavelength are then calculated as a function of phase and amplitude of facet reflection. The effects of the power lost via radiation from the surface are also calculated.

## 2 Theory

The electric field  $E(x, z)$  propagating in a waveguide with periodic corrugations is given by [20–23]

$$E(x, z) = [R(z) \exp(i\beta_0 z) + S(z) \exp(-i\beta_0 z)]E_0(x) \quad (1a)$$

where  $E_0(x)$  describes the transverse field profile. For a second order grating, the longitudinal propagation constant is  $\beta_0 = 2\pi/\Lambda$ , where  $\Lambda$  is the period of the grating. The functions  $R(z)$  and  $S(z)$  represent the right and left propagating mode amplitudes in the waveguide, respectively. In addition, the radiation field profile is assumed to have a similar  $z$  dependence, i.e.

$$E_{-1}(x, z) = [R(z) + S(z)]E_{-1}(x) \quad (1b)$$

where  $E_{-1}(x)$  is the transverse profile of the radiation field. Notice that eqn. 1b is only true for symmetrical grating 'tooth shapes'. From the above assumptions, the coupled wave equations for  $R(z)$  and  $S(z)$  can be obtained (as given by [20–22])

$$\frac{dR}{dz} = (g + i\Delta\beta - h_1)R + i(K + ih_1)S + i, \quad (2a)$$

$$\frac{dS}{dz} = -(g + i\Delta\beta - h_1)S - i(K + ih_1)R + i, \quad (2b)$$

where  $h_1$  is the surface diffraction loss coefficient and  $K$  is the longitudinal grating coupling coefficient [20–22].  $\Delta\beta$  is the deviation from the Bragg condition.  $i_r$  and  $i_s$  are the spontaneous fields coupled to the forward and reverse propagating waves. The net amplitude gain (in  $\text{cm}^{-1}$ ) for the propagating waves is

$$\frac{1}{2} \left[ \frac{\Gamma a(N - N_0)}{(1 + \epsilon P)} - \alpha \right] \quad (3a)$$

where  $a$  is the differential gain,  $P$  is the photon density and  $\Gamma$  is the confinement factor.  $N_0$  is the carrier concentration at transparency.  $\epsilon$  is the gain compression factor. The loss factor caused by free electron absorption and other distributed losses is given by  $\alpha$ . The carrier induced index change related to the differential gain is given by

$$\Delta n = -\frac{\alpha_H \lambda_0}{4\pi} \Gamma a(N - N_{th}) \quad (3b)$$

where  $\alpha_H$  is the 'Henry's  $\alpha$  factor' and  $N_{th}$  is the threshold carrier concentration. The change in effective refractive

index  $n_{eff} = n_{eff_0} + \Delta n$  (where  $n_{eff}$  is the refractive index when carrier density is  $N_0$ ). Since only a small change in  $\beta$  is caused by the change in refractive index, we can deduce the complex part of the field gain from eqn. 3b.

The nonuniform distribution of carrier and photon density can be solved by splitting the laser into cascaded sections. Using the power matrix method [19], the field distribution can be calculated. The behaviour of the laser (including longitudinal effects), is described by a carrier rate equation for each section, i.e.

$$\frac{dN}{dt} = \frac{J}{gd} - BN^2 - CN^3 - v_g \sum_i \frac{d(N - N_0)P_i}{(1 + \epsilon P_i)} \quad (4)$$

where  $B$  is the bimolecular carrier recombination coefficient,  $C$  is the Auger recombination coefficient,  $v_g$  is the group velocity,  $J$  is the injection current density,  $d$  is the active layer thickness and  $i$  is the mode number of the emission spectrum.

From eqn. 1b, the near field profile in the longitudinal direction is the sum of right and left propagating fields [1–4]:

$$E(z)_{near} = [R(z) + S(z)] \quad (5)$$

The near field given in eqn. 5 can be converted into a power matrix format and is given by

$$E_{near} = GV_n = \begin{bmatrix} R_n + S_n \\ 0 \end{bmatrix} \quad (6a)$$

where  $V_n$  is given in Appendix 7 and  $G$  is given as

$$G = \begin{bmatrix} 1 & 1 \\ 0 & 0 \end{bmatrix} \quad (6b)$$

The relative surface radiation from each section of the laser is given by

$$|R_n(z) + S_n(z)|^2 = (GV_n)^+ GV_n = U_n(z)^+ U_n(z) \quad (7)$$

where the expression for  $U_n(z)$  is given in Appendix 7. The  $^+$  represents the complex conjugate and transpose.

The far field amplitude versus angular deviation ' $\Theta$ ' from the surface normal in the longitudinal direction is found by taking the Fourier transform of the near field amplitude and multiplying by an obliquity factor  $\cos \Theta$ , hence

$$F(\Theta) \sim \cos \Theta \int_{-z}^z [R(z) + S(z)] \exp[-ik_0 \sin(\Theta)z] dz \quad (8)$$

The effects of reflection from the semiconductor–air interface are neglected. Substituting eqn. 6 into eqn. 8 and then integrating within each section, we obtain

$$F(\Theta) \sim \cos(\Theta) \sum_{n=0}^M \int_0^{\delta z_n} W_n(z) \exp[-ik_0 \sin(\Theta)z] dz \quad (9)$$

where  $\delta z_n$  is the length of the  $n$ th section,  $z' = z + (n - M/2)\delta z_n$  and the matrix  $W_n(z)$  can be written as

$$W_n(z) = \begin{cases} GT_i(z)V_0 & \text{for } n = 1 \\ GT_n(z) \prod_{i=1}^{n-1} T_i(\delta z_i)V_0 & \text{for } n > 1 \end{cases} \quad (10)$$

and  $W_0 = GV_0$ . The value of  $|V_0|^2$  can be obtained by the power matrix method [19]. The value of  $|F(\Theta)|^2$  can be compute numerically.

### 3 Results

In our calculations, we assume  $KL = 2$ , where  $L$  is the length of the laser, the values of  $h_1$  and  $K$  are given as  $h_1 = 4.5 \text{ cm}^{-1}$  and  $K = 50 \text{ cm}^{-1}$ . Values of the other parameters used in this analysis are listed at the start of the pages. Fig. 1 shows the schematic structure of the laser with left and right end facet reflections given by

$$\rho_l \exp(i2\pi\phi_l) \text{ and } \rho_r \exp(i2\pi\phi_r) \quad (11)$$

$\rho_i$  is the amplitude of reflection and  $\phi_i$  is the normalised phase, where  $i = l, r$ .

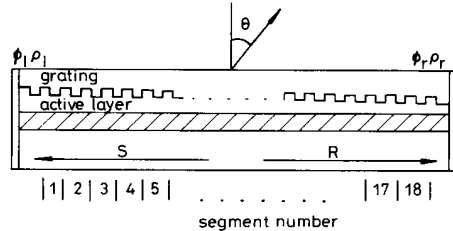


Fig. 1 Schematic structure of SEDFB laser

$\rho_l, \rho_r, \phi_l, \phi_r$  = amplitude and phase of left-hand and right-hand facet.  $\theta$  = angle of beam deflection from surface normal

#### 3.1 General solutions

Figs. 2 and 3 show the surface emitted beam profiles and longitudinal variation of carrier and photon density of a SEDFB laser with asymmetric coating under uniform injection. The laser is divided into 18 sections with an antireflection (AR) coating on the left end facet ( $\rho_l = 0$ ) and a high reflection (HR) coating on the other facet. We assume that the magnitude of amplitude reflectivity of the HR coating is equal to 80% ( $\rho_r = 0.80$ ). In Fig. 2, the phase of the HR coating is assumed to be equal to zero ( $\phi_r = 0$ ). Spatial hole burning is observed from the longitudinal carrier density distribution shown in Fig. 2A.

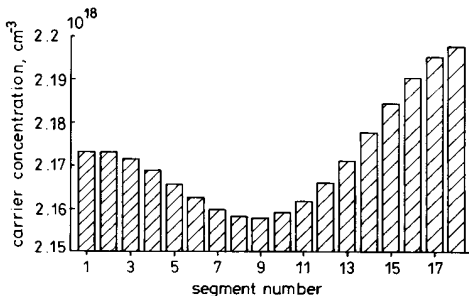


Fig. 2A Longitudinal carrier distribution

$\rho_l = 0, \rho_r = 0.8, \phi_r = 0$

Higher optical intensity is observed near the AR facet than near the HR one, as shown in Fig. 2B. The near field profile given in Fig. 2C indicates a null near the centre of the laser. This is caused by destructive interference from the forward and backward propagating waves. The far field profile corresponding to Fig. 2C is double lobed and is given in Fig. 2D. An asymmetric near field profile is caused by feedback from the HR coating, and Fig. 2E shows a corresponding emission spectrum

spectrum. In Fig. 3, the phase of the HR coating is changed to be equal to  $250^\circ$  ( $\phi_r = 0.7$ ). In this case, the carrier concentration increases monotonically (see Fig. 3A) in the longitudinal direction. The longitudinal

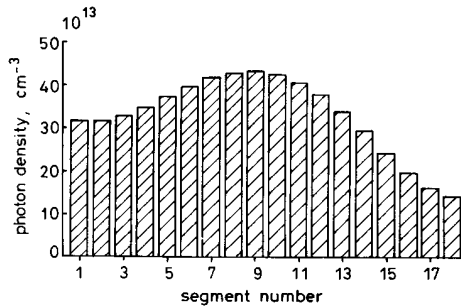


Fig. 2B Longitudinal photon distribution

$\rho_l = 0, \rho_r = 0.8, \phi_r = 0$

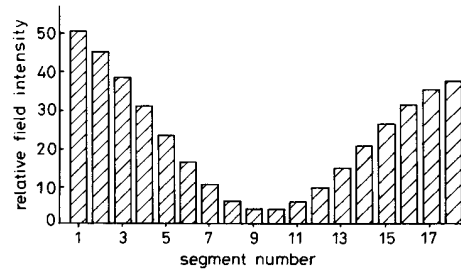


Fig. 2C Longitudinal near field pattern

$\rho_l = 0, \rho_r = 0.8, \phi_r = 0$

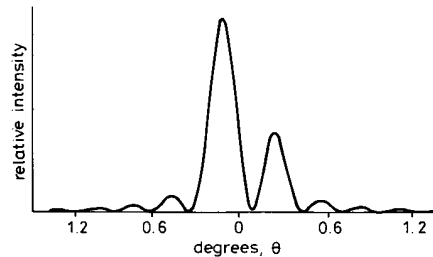


Fig. 2D Far field radiation pattern

$\rho_l = 0, \rho_r = 0.8, \phi_r = 0$

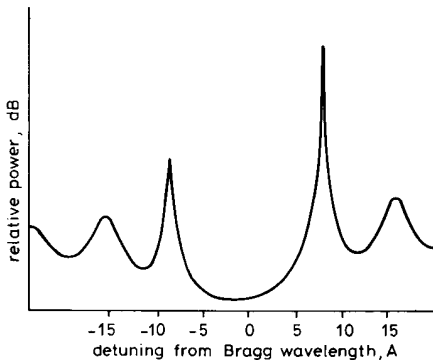
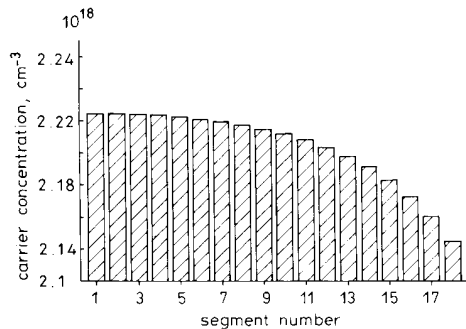


Fig. 2E Emission spectrum

$\rho_l = 0, \rho_r = 0.8, \phi_r = 0$

photon density and near field distributions given in Fig. 3B and 3C are seen to have similar shapes to the carrier concentration. High radiation intensity occurs near the facet with the HR coating. Fig. 3D shows the single lobed radiation pattern calculated from this near field profile. Its spectrum is shown in Fig. 3E.



**Fig. 3A** Longitudinal carrier distribution

$\rho_1 = 0, \rho_r = 0.8, \phi_r = 0.7$

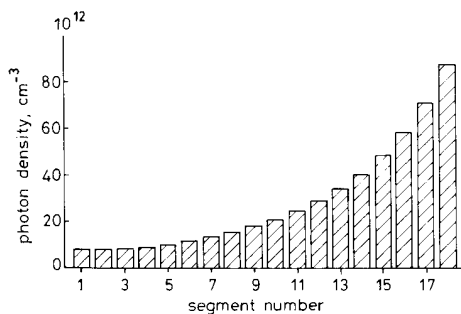


**Fig. 3B** Longitudinal photon distribution

$\rho_1 = 0, \rho_r = 0.8, \phi_r = 0.7$

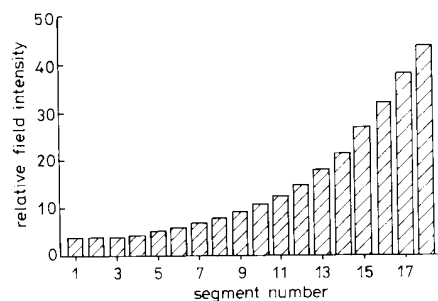


**Fig. 3C** Longitudinal near field pattern

$\rho_1 = 0, \rho_r = 0.8, \phi_r = 0.7$

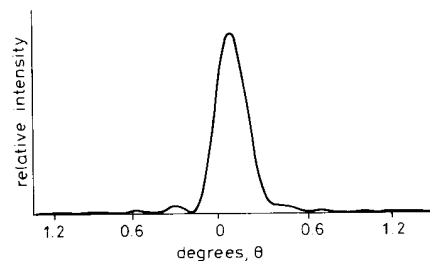


**Fig. 3D** Far field radiation pattern

$\rho_1 = 0, \rho_r = 0.8, \phi_r = 0.7$

The only difference between Figs. 2B and 3B is the phase of the HR facet. The facet phase modifies the relative phase between the forward and reverse fields, and as a result changes the photon density distribution. In addition, the oscillation detuning from the Bragg wavelength is also changed by the facet phase, and the far field is

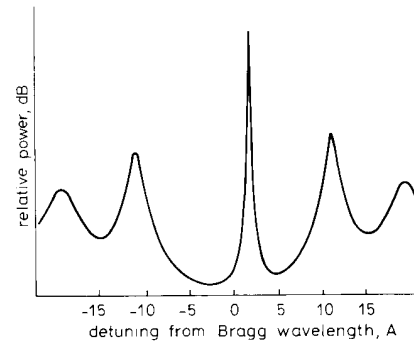


**Fig. 3E** Emission spectrum

$\rho_1 = 0, \rho_r = 0.8, \phi_r = 0.7$

double or single lobed depending on this phase. The deviation of the lasing wavelength from the Bragg wavelength results in a beam deflection  $\Theta$  from the surface normal which can be approximated as

$$\Theta = \pm \sin^{-1}[\Delta\beta/(2\pi/\lambda_0)] \quad (12)$$

where the + and - signs represents forward and reverse fields. From eqn. 12, we expect that, as the oscillation frequency nears the Bragg frequency, the two peaks will overlap and a single lobed far field will be obtained. Alternatively, if the deviation is increased, the double peaks will move further apart.

This simple physical explanation of far field shapes cannot be applied to many more complex structures, most obviously those with  $\lambda/4$  phase shifts where  $\Delta\beta$  is often zero, so that eqn. 12 does not apply directly. In fact, by using arguments of symmetry and phase matching, a DFB laser with a central  $\lambda/4$  phase shift and both facets AR coated can be seen to have a far field similar to that shown in Fig. 2C but symmetric. In still more complex structures, physical arguments become very complex indeed, but the model of course continues to give the correct far fields.

### 3.2 Effect of facet reflectivity on surface radiation

In the following calculations, the laser is divided into ten sections to reduce computing time. Although some error will be introduced, the characteristics of the far field profiles of interest change little.

Fig. 4 shows the far field radiation profile with several different asymmetric coating configurations. The left-hand facet always has zero reflectivity ( $\rho_1 = 0$ ). The magnitude of the right-hand facet reflectivity ( $\rho_r$ ) increases from 0 to 1 from the bottom to top of the Figure, and its phase is set to ( $\phi_r = 0.1$ ). The total radiated power from the surface is kept constant, and uniform current injection is assumed. As might be expected, the amplitude difference of the two peaks increases with facet reflection. Beam deflection from normal is also slightly changed by the facet reflection. Using eqn. 12, and taking  $\lambda_0 = 1.55 \mu\text{m}$ ,  $\Delta\beta = 84 \text{ cm}^{-1}$  (corresponding to  $8.5 \text{ \AA}$ ), we obtain approximate beam deflections  $\Theta = \pm 0.12^\circ$  which are close to the results in Fig. 4 obtained by more exact

calculation. Varying the drive current has only a small effect on the output beam characteristics, these being essentially unchanged, although there are subtle variations in the far field lobe widths and spacings.

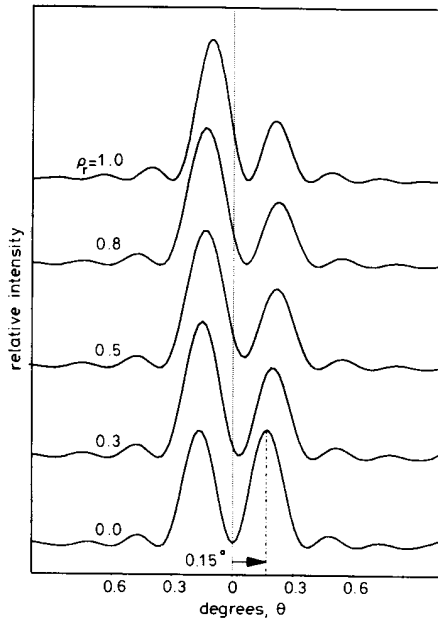


Fig. 4 Effect of facet reflectivity on far field pattern  
 $h_1 = 4.5/\text{cm}$ ,  $\rho_1 = 0.0$ ,  $\phi = 0.1$

### 3.3 Effects of facet phase on surface radiation

Fig. 5a shows the effect of right-hand facet phase ( $\phi_r$ ) on wavelength for phases from 0 to 1 (normalised to  $2\pi$ ), and for reflectivities of 0.3, 0.5, 0.8 and 1.0. The left-hand facet has zero reflectivity and so its phase is arbitrary.

It can be seen from  $\rho_r = 1.0$  that the wavelength is predominantly near the upper boundary of the stopband, but, approaching  $\phi_r = 1$ , it shifts smoothly to the lower side, and then shifts back again abruptly at  $\phi_r = 0.05$ .  $\rho_r = 0.8$  gives similar results, but the abrupt switch back to the upper side occurs sooner. In both cases, between  $\phi_r = 0.5$  and 0.8, a mode is being excited within the stopband. The spectrum is similar to that given in Fig. 3D. The abrupt switch at  $\phi_r = 0.05$  and 0.8 is when the lasing mode jumps to the other side of the stopband. With  $\rho_r = 0.5$ , the behaviour becomes more complex, with abrupt switches both to the lower side of the stopband and back again. Similar results are observed at  $\rho_r = 0.3$ . The higher threshold gains necessary with lower reflectivity ( $\rho_r = 0.3$  and 0.5) facets remove the possibility of stopband modes.

In fact, the wavelength behaviour is somewhat more complex than shown. The facet phase clearly affects lasing threshold depending whether it causes constructive or destructive interference (as shown in Fig. 5b). This varying threshold causes changes in the Bragg wavelength via carrier induced refractive index change. To make the laser's behaviour clearer, we have normalised the wavelengths in Fig. 5a to the shifted Bragg wavelength.

Corresponding to Fig. 5a for wavelength, Fig. 6a and b show, respectively, the far and near fields for surface emission with  $\rho_r = 1.0$  and  $\phi_r$  variable. Fig. 6c, 6d and 6e give corresponding far fields for  $\rho_r = 0.8, 0.5$  and 0.3,

respectively. Note that, while true single lobed patterns are seen, a broad single lobe can occur where two lobes have coalesced. This is seen in Fig. 6a for  $\phi_r = 0.5$ , in Fig. 6c for  $\phi_r = 0.48$ . This can be explained by the argument

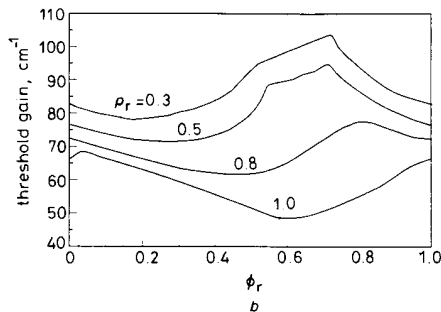
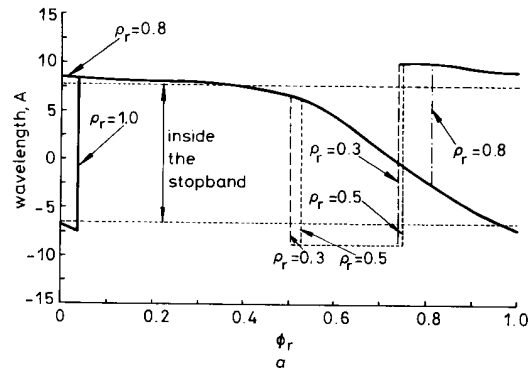


Fig. 5 Effect of right-hand facet phase  $\phi_r$   
a on wavelength,  $\phi_r$  vary from 0 to 1 (normalised to  $2\pi$ ) with reflectivities  $\rho_r = 0.3, 0.5, 0.8$  and 1.0;  $\rho_1 = 0.0$ ,  $h_1 = 4.5/\text{cm}$   
b on threshold gain,  $\phi_r$  vary from 0 to 1 (normalised to  $2\pi$ ) with reflectivities  $\rho_r = 0.3, 0.5, 0.8$  and 1.0;  $\rho_1 = 0.0$ ,  $h_1 = 4.5/\text{cm}$

given after eqn. 12. In Fig. 6a, at  $\phi_r = 0.5$ , the full width half maximum (FWHM) of the far field is a maximum, but it reduces at  $\phi_r = 0.7$  and then slightly increases again at  $\phi_r = 1.0$ . Similar behaviour is observed in Fig. 6c but not in Figs. 6d and e. Comparing the beam deflection angles of the single lobes in Figs. 6a and c with those of Figs. 6d and e, they are on opposite sides of the normal ( $\Theta = 0$ ). This implies that single lobe patterns form in Fig. 6d and e are caused by a combination of high deviation wavelength and facet reflection, which is not readily apparent from eqn. 12.

Figs. 7a and b show far fields for symmetric lasers with  $\rho_r = \rho_1 = 0.8$  and 0.5, respectively and  $\phi_1 = 0$  in all cases. Both single and double lobed patterns are seen, but the range of single lobed behaviour is reduced when compared with the asymmetric examples.

### 3.4 Surface scattering loss and spontaneous emission

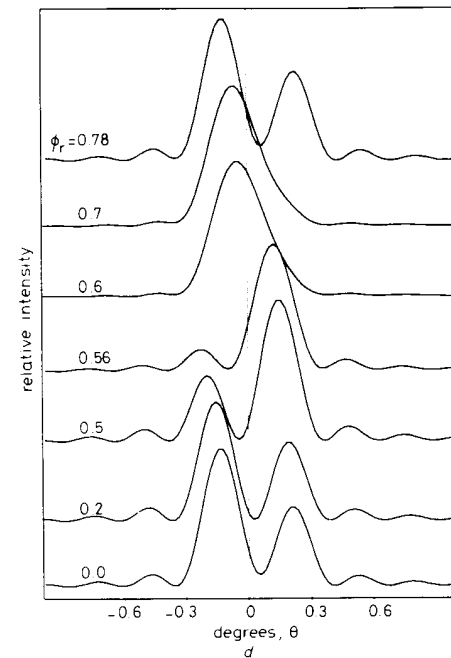
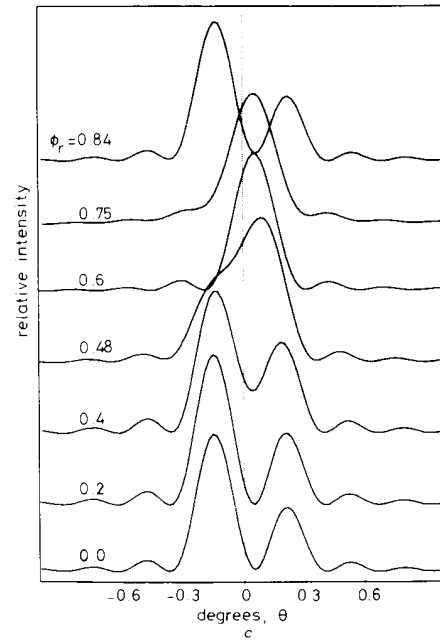
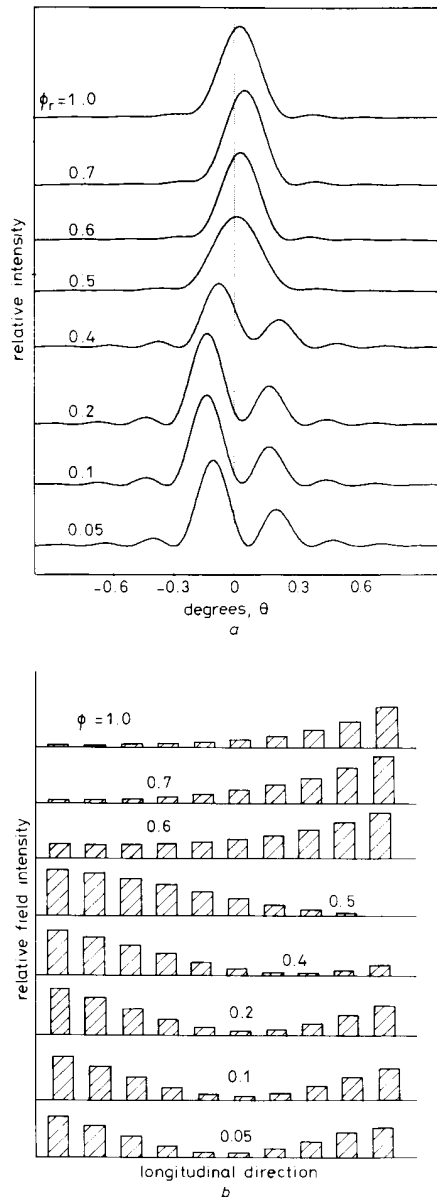
Further calculations have been done which indicate that if the surface loss (= radiation) coefficient  $h_1$  [20-22] is increased to 9.0 or 13.5  $\text{cm}^{-1}$ , the range of single lobed far fields is reduced. This is because the threshold gain is increased by the surface radiation loss, and the allowable phase range to excite a bandgap mode is reduced. However, the field profiles are essentially similar to those of Fig. 6 and hence are not repeated. We have assumed that the coupling coefficient  $K$  remains constant for these calculations concerning increased surface loss.

There are two possible ways in which spontaneous emission can affect the far field profiles: (i) spontaneous emission coupled into the lasing modes broadens these modes spectrally, and hence far field profiles are also broadened (spatially); (ii) spontaneous emission is radiated uniformly along the active region within the angle of total internal reflection. Both effects contribute to far field broadening below, and just above threshold, but spontaneous effects are negligible well above threshold.

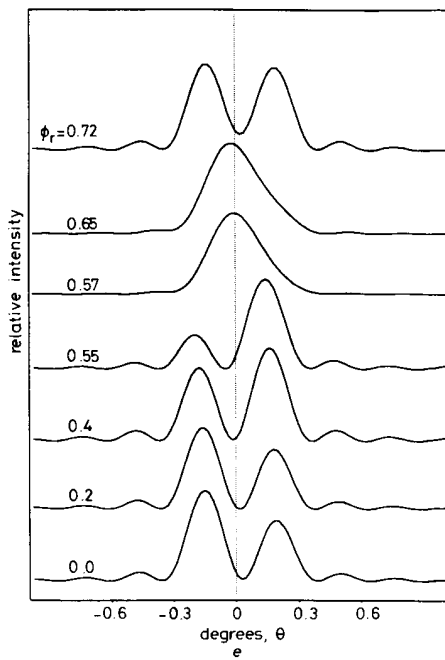
#### 4 Experimental results

To illustrate the results from our analysis, we have tested the far field radiation profile of a SEDFB laser under the

influence of strong external optical feedback. The experimental setup is shown in Fig. 8A. A  $1.55 \mu\text{m}$  second order DFB laser with both facets AR coated was used in the experiment. The laser was mounted *p*-side down on a



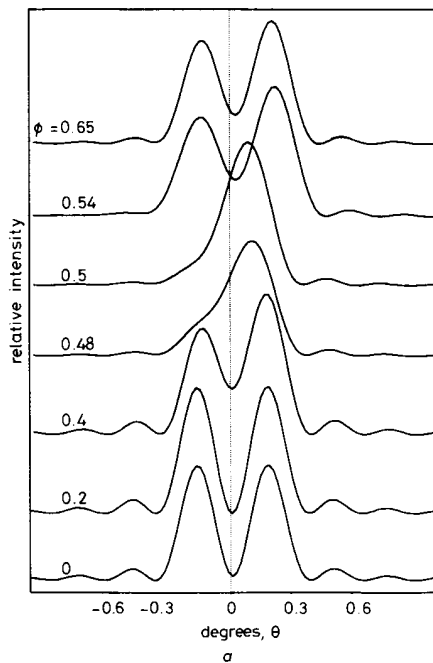
**Fig. 6** Effect of right-hand facet phase  
*a* on far field  $h_1 = 4.5/\text{cm}$ ,  $\rho_1 = 0.0$ ,  $\rho_r = 1.0$   
*b* on near field  $h_1 = 4.5/\text{cm}$ ,  $\rho_1 = 0.0$ ,  $\rho_r = 1.0$   
*c* on far field  $h_1 = 4.5/\text{cm}$ ,  $\rho_1 = 0.0$ ,  $\rho_r = 0.8$   
*d* on far field  $h_1 = 4.5/\text{cm}$ ,  $\rho_1 = 0.0$ ,  $\rho_r = 0.5$



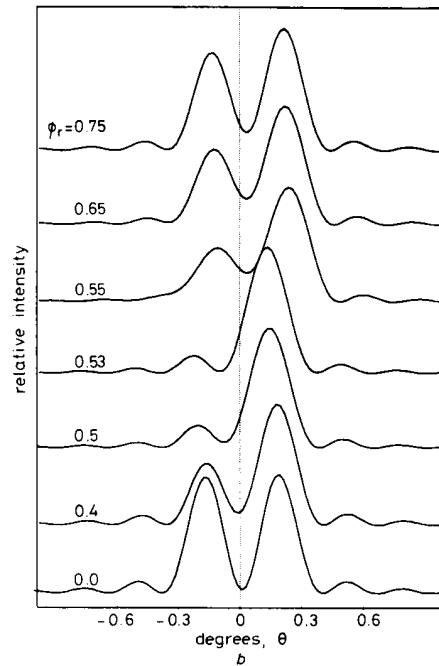
**Fig. 6** (Cont)  
*e* on far field  $\rho_1 = 0.0$ ,  $\rho_r = 0.3$

diamond heat sink, and the metallisation on the *n*-side was partly removed to form an output window. External optical feedback to one facet was provided by a mirror and a ball lens. The radius of the ball lens was  $150 \mu\text{m}$ , and it was glued directly to a plane gold mirror. The mirror-lens assembly was adjusted in *x*, *y*, *z* to maximise reflected coupled power; this results in the ball lens almost touching the laser facet. Power from the other facet was monitored by an InGaAs photodiode. The far field pattern of the surface emission was measured on the faceplate of an infrared camera positioned 10–20 cm from the device. The phase of the reflected wave could be changed by moving the mirror slightly in the longitudinal direction. This was achieved using a piezo electric translator with resolution of the order of  $0.01 \mu\text{m}$ . With the laser operating in the same mode (i.e. no large changes in wavelength or far field) a maximum reduction of 10% in threshold due to the reflection could be observed. Matching these results to the model suggests an effective reflectance of  $0.2 < \rho < 0.35$  for the mirror-lens combination.

Fig. 8*b* shows the far field profile with the signal received from the photodiode maximised. The two lobes of the far field are distinct. However, when we minimise the signal by moving the mirror, the far field changes so that the right-hand lobe grows and the other lobe shrinks, and they also move closer together (see Fig. 8*c*). In this experiment, the 'tuning angle' of the far field is limited because the effective field coupling back into the laser is only about 30%. These results are qualitatively consistent with the theoretical results given before (see. 6*e* at  $\phi_r$  between 0.2 and 0.5).



**Fig. 7** Effect of right-hand facet phase  
*a* on far field  $\phi_1 = 0$ ;  $h_1 = 4.5/\text{cm}$ ,  $\rho_1 = 0.8$ ,  $\rho_r = 0.8$   
*b* on far field  $\phi_1 = 0$ ;  $h_1 = 4.5/\text{cm}$ ,  $\rho_1 = 0.5$ ,  $\rho_r = 0.5$



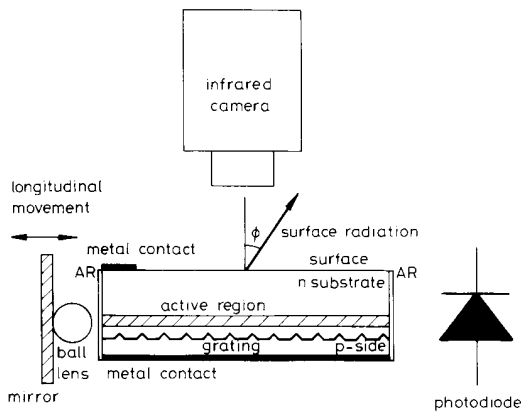


Fig. 8A Experimental setup to measure far field radiation profile diagram is not to scale

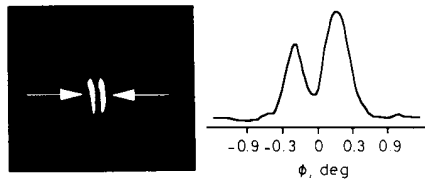


Fig. 8B Magnified image of far field profile observed on camera with maximum photodiode current

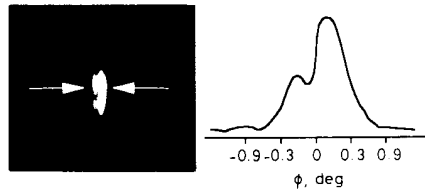


Fig. 8C Magnified image of far field profile observed on camera with minimum photodiode current

## 5 Conclusions

In conclusion, we have developed a method for modelling grating coupled distributed feedback lasers. Using this model, we show that the probability of a single lobed radiation pattern can be enhanced by HR coating one facet, and AR coating the other. The radiation profile is seen to be a function of threshold gain and facet reflection, as well as deviation from the Bragg wavelength. Predictions from the analysis are consistent with limited results obtained experimentally.

## 6 References

- MACOMBER, S.M.: 'Nonlinear analysis of surface-emitting distributed feedback lasers', *IEEE J.*, 1990, **QE-26**, (12), pp. 2065-2074
- HARDY, A., WELCH, D.F., and STREIFER, W.: 'Analysis of second order gratings', *IEEE J.*, 1989, **QE-25**, (10), pp. 1989-2105
- HARDY, A., WAARTS, R.G., WELCH, D.F., and STREIFER, W.: 'Analysis of three-grating coupling surface emitters', *IEEE J.*, 1990, **QE-26**, (5), pp. 843-849

- AMANTEA, R., CARLSON, N.W., PALFREY, S.L., EVANS, G.A., HAMMER, J.M., and LURIE, M.: 'Network analysis of the modes of two-dimensional grating-surface-emitting diode laser array', *IEEE J.*, 1990, **QE-26**, (6), pp. 1023-1038
- MACOMBER, S.H., MOTT, J.S., NOLL, R.J., GALLATIN, G.M., GRATIX, E.J., O'DWYER, S.L., and LAMBERT, S.A.: 'Surface-emitting distributed feedback semiconductor laser', *Appl. Phys. Lett.*, 1987, **51**, (7), pp. 472-474
- MITSUNAGE, K., KAMEYA, M., KOJIMA, K., NODA, S., KYUMA, K., HAMANAKA, K., and NAKAYAMA, T.: 'CW surface-emitting grating-coupled GaAs/AlGaAs distributed laser with very narrow beam divergence', *Appl. Phys. Lett.*, 1987, **50**, (25), pp. 1788-1790
- KOJIMA, K., NODA, S., MITSUNAGE, K., KYUMA, K., HAMANAKA, K., and NAKAYAMA, T.: 'Edge- and surface-emitting distributed Bragg reflector laser with multiquantum well active/passive waveguide', *Appl. Phys. Lett.*, 1987, **50**, pp. 227-229
- CARLSON, N.W., EVANS, G.A., HAMMER, J.M., LURIE, M., PALFREY, S.L., and DHOLAKIA, A.: 'Phase-locked operation of a grating-surface-emitting diode laser array', *Appl. Phys. Lett.*, 1987, **50**, pp. 1301-1303
- EVANS, G.A., CARLSON, N.W., HAMMER, J.M., LURIE, M., BUTTER, J.K., PALFREY, S.L., AMANTEA, R., CARR, L.A., HAWRYLO, F.Z., JAMES, E.A., KAISER, C.J., KIRK, J.B., REICHERT, W.F., CHINN, S.R., SHEALY, J.R., and ZORY, P.S.: 'Coherent monolithic two-dimensional (10 x 10) laser arrays using grating surface emission', *Appl. Phys. Lett.*, 1988, **53**, pp. 2123-2125
- CARLSON, N.W., EVANS, G.A., HAMMER, J.M., LURIE, M., CARR, L.A., HAWRYLO, F.Z., JAMES, E.A., KAISER, C.J., KIRK, J.B., REICHERT, W.F., TRUXAL, D.A., SHEALY, J.R., CHINN, S.R., and ZORY, P.S.: 'High power seven-element grating surface emitting diode laser array with 0.012° far-field angle', *Appl. Phys. Lett.*, 1988, **52**, pp. 939-941
- WELCH, D.F., PARKE, R., HARDY, A., STREIFER, W., and SCIFES, D.R.: 'High power grating coupled surface emitters', *Electron. Lett.*, 1989, **25**, pp. 819-820
- NAGATA, H., KOMABA, N., and YAMASHITA, K.: 'AlGaAs grating surface emitting beam deflector with ridge structure', *IEEE Photon. Technol. Lett.*, 1991, **3**, pp. 222-224
- NAGATA, H., KOMABA, N., and YAMASHITA, K.: 'AlGaAs grating surface emitting beam deflector utilizing carrier-induced refractive index change', *Appl. Phys. Lett.*, 1990, **56**, pp. 1299-1301
- 'Special issue on optical interconnects', *Optical and Quantum Electronics*, **24**, (4), see papers of this issue
- NEFF, J.A.: 'Major initiatives for optical computing', *Opt. Eng.*, 1987, **26**, (2), pp. 2-9
- HARTMANN, A., and REDFIELD, S.: 'Design sketches for optical crossbar switches intended for large scale parallel processing application', *Opt. Eng.*, 1988, **28**, (4), p. 315
- CHIANG, H.K., KENAN, R.P., and SUMMERS, C.J.: 'The analysis of a phase-delayed optical two state switch', *IEEE Photon. Technol. Lett.*, 1992, **4**, pp. 368-370
- KUZNETSON, H.: 'Theory of wavelength tuning in two-segment distributed feedback lasers', *IEEE J.*, 1988, **QE-24**, pp. 1837-1844
- ZHANG, L.M., and CARROLL, J.E.: 'Large signal dynamic model of the DFB laser', *IEEE J.*, 1992, **QE-28**, (3) pp. 604-611
- STREIFER, W., SCIFRES, D.R., and BURNHAM, R.D.: 'Coupled wave analysis of DFB and DBR laser', *IEEE J.*, 1977, **QE-13**, (4), pp. 134-141
- STREIFER, W., SCIFRES, D.R., and BURNHAM, R.D.: 'Analysis of grating-coupled radiation in GaAs:GaAlAs lasers', *IEEE J.*, 1976, **QE-12**, (7), pp. 422-428
- KAZARINOV, R.F., and HENRY, C.H.: 'Second-order distributed feedback lasers with mode selection provided by first order radiation losses', *IEEE J.*, 1985, **QE-21**, (2), pp. 144-150

## 7 Appendix

The travelling waves amplitudes in section  $n$  ( $R_n$  and  $S_n$ ) are written in vector notation:

$$V_n = \begin{bmatrix} R_n \\ S_n \end{bmatrix} \quad (13)$$

From eqn. 13,  $V_0$  can be expressed as

$$V_0 = [d][K]^{-1} \sum_{m=1}^{M-1} S^{m+1} J_m \quad (14)$$

where  $[k]$ ,  $[d]$ ,  $S$  and  $I_m$  are defined in Reference 19.  $U_0$  can be obtained from multiplying  $V_0$  by  $G$ :

$$U_0 = G[d][K]^{-1} \sum_{m=1}^{M-1} S^{(m+1)} I_m \quad (15)$$

and

$$\begin{aligned} |U_0|^2 &= [0 \quad (R_0 + S_0)^*] \begin{bmatrix} 0 \\ (R_0 + S_0) \end{bmatrix} \\ &= \sum_{j=1}^{M-1} \sum_{i=1}^{M-1} I_j^+ S^{(j+1)*} [K]^{-1*} \\ &\quad \times [d]^+ G^+ G[d][K]^{-1} S^{(i+1)} I_i \end{aligned} \quad (16)$$

Because the spontaneous field is incoherent, the following relationships hold:

$$i_{rj} i_{ri} = i_r^2 \delta_{ji}, \quad i_{sj} i_{si} = i_s^2 \delta_{ji}, \quad i_{rj} i_{si} = i_{sj} i_{ri} = 0 \quad (17)$$

therefore eqn. 16 can be simplified to

$$\begin{aligned} |U_0|^2 &= \sum_{k=1}^{M-1} \text{trace} (Y_k^+ Y_k) I_k^2 \\ &= \sum_{k=1}^{M-1} \sum_{1,2} |Y_k|_{1,2}^2 I_k^2 \end{aligned} \quad (18)$$

where  $Y_k = G[d][K]^{-1} S^{(k+1)}$ ,  $I_k^2 = i_{rk}^* i_{rk} = i_{sk}^* i_{sk}$ .

Powers of the sum of forward and reverse waves in each section  $|U_n|^2$  can be calculated in a similar way as  $|U_0|^2$ .